# Direct Encoding of Tunable Stiffness Into an Origami-Inspired Jumping Robot Leg

## **Fuchen Chen**

Ira A. Fulton Schools of Engineering, Arizona State University, Mesa, AZ 85212 e-mail: fchen65@asu.edu

## Daniel M. Aukes<sup>1</sup>

Ira A. Fulton Schools of Engineering, Arizona State University, Mesa, AZ 85212 e-mail: danaukes@asu.edu The stiffness of robot legs greatly affects legged locomotion performance; tuning that stiffness, however, can be a costly and complex task. In this paper, we directly tune the stiffness of jumping robot legs using an origami-inspired laminate design and fabrication method. In addition to the stiffness coefficient described by Hooke's law, the nonlinearity of the force-displacement curve can also be tuned by optimizing the geometry of the mechanism. Our method reduces the number of parts needed to realize legs with different stiffness while simplifying manual redesign effort, lowering the cost of legged robots while speeding up the design and optimization process. We have fabricated and tested the leg across six different stiffness profiles that vary both the nonlinearity and coefficient. Through a vertical jumping experiment actuated by a DC motor, we also show that proper tuning of the leg stiffness can result in an 18% improvement in lift-off speed and an increase of 19% in peak power output. [DOI: 10.1115/1.4056958]

Keywords: compliant mechanisms, folding and origami, legged robots, mechanism design

#### 1 Introduction

Tunable leg compliance can be beneficial for applying legged robots to tasks that require both an understanding of and optimization for niche tasks. This paper introduces a method for tuning the stiffness coefficient and nonlinearity of compliant mechanisms for robot legs with the help of origami-inspired laminate design and fabrication methods.

In biology, leg stiffness is an important part of the study and characterization of legged organisms [1–3]. Tuned stiffness has also been incorporated into robotic leg designs, demonstrating benefits such as passive stability, improved running speed, lower cost of transport, and increased peak power output [4–10]. It is also shown that operating payload, terrain, and speed of a robot have great impact on the optimum leg stiffness [11]. Although most literature considers leg stiffness as linear—only designing and tuning a constant stiffness coefficient using Hooke's law—locomotion performance is in fact additionally affected by the nonlinear behavior of leg compliance. Springs with "strain-softening" force-displacement curves have been shown to improve jumping air time and height [12,13]. Furthermore, it has been shown from a theoretical perspective that running speed and stability can also benefit from spring nonlinearity [14,15].

Three main approaches are employed in the literature for tuning and integrating leg stiffness. First of all, the stiffness can be provided by discrete spring elements: rubber or latex tubes [5,16], fiberglass plates [9,17], or off-the-shelf metal springs [7,10]. While being the most straightforward and conventional way, this method often requires additional connectors and fasteners for the springs, adding mass and design complexity. The leg may also need to be manually re-designed when switching springs or changing stiffness. The stiffness range of some springs can be limited by commercial availability; customization can also be difficult and costly.

On the other hand, motors at the leg joints can mimic the dynamics of springs through control algorithms such as virtual

model control [18] and impedance control [19] to provide appropriate and tunable stiffness and even damping. Unfortunately, the sensing and computing power required increase the cost and complexity of the robots. Furthermore, this method has poor energy storage efficiency and actuation bandwidth compared to physical springs [9]. Interestingly, the repulsion force between permanent or electromagnetic magnets can also be directly utilized as a spring as demonstrated in the development of variable stiffness joints [20–22], which might have potentials in legged robots

Finally, the leg mechanisms can be directly made of compliant materials namely plastic sheets [23], carbon fiber strips [13], and even cardboard [6] so that both the motion and stiffness requirements are met, which reduces cost, saves weight, and provides greater stiffness design freedom. However, this approach adds more difficulty to the design phase, requiring knowledge of the material properties, extensive simulation and testing, and compact fabrication of mechanisms. Moreover, this approach is less studied in the literature despite its great potential in low-cost and small-scale legged robots.

We suggest that origami-inspired laminate devices [24] make it possible to affordably tune the stiffness of cm-scale legged robots as illustrated in Fig. 1. The fabrication of laminate devices is shown in Fig. 2. At first, layers of materials are individually cut into patterns with a laser cutter and laminated together with a laminate machine. Then, after the scrap and support material are removed by a release cut, the devices are then folded and locked into places with staples. This fabrication technique, similar to traditional origami, creates three-dimensional mechanisms through folding up flat sheets of materials and it also extends the convention by including cutting and multi-layer lamination to accommodate robotic needs, which leads to multiple benefits applicable to designing and building legged robots. Since the materials most commonly used with laminate fabrication processes exhibit inherent compliance at these scales, a wide range of tunable stiffness profiles can be directly encoded into legged mechanisms. Tight integration reduces costs by eliminating parts and saves time during assembly. Furthermore, the dynamics of the device may then be naturally parameterized by the geometries of its constituent links, making it straightforward to combine and automate surrounding design and fabrication processes.

<sup>&</sup>lt;sup>1</sup>Corresponding author.

Contributed by Mechanisms and Robotics Committee of ASME for publication in the JOURNAL OF MECHANISMS AND ROBOTICS. Manuscript received August 6, 2022; final manuscript received February 8, 2023; published online March 29, 2023. Assoc. Editor: Hao Su.

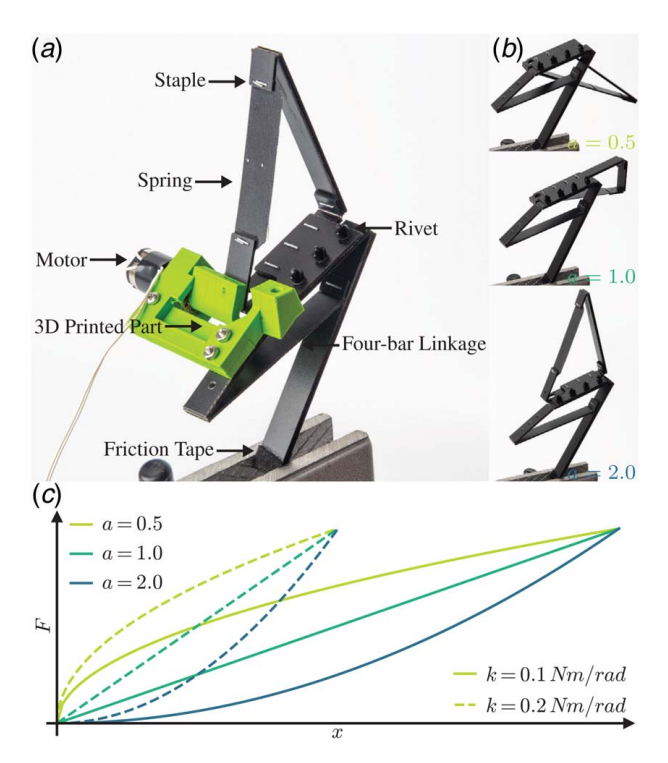


Fig. 1 (a) Photo of the laminate robot leg, (b) photos of the leg tuned to different stiffness nonlinearity factors, which correlate with the leg's geometry, and (c) examples of stiffness profiles of the leg

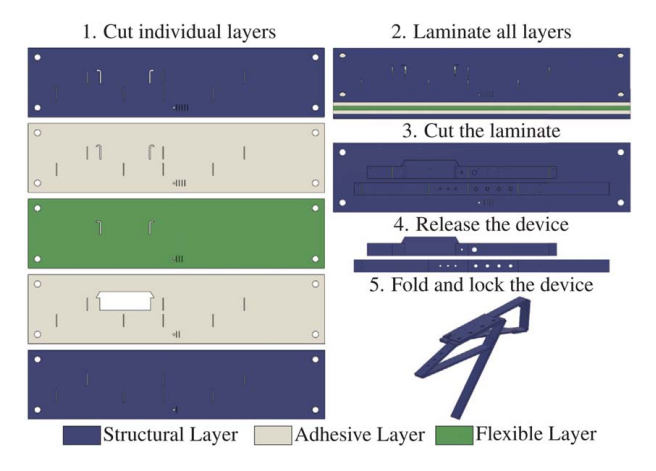


Fig. 2 The origami-inspired laminate fabrication process

The contributions of this paper are as follows: (1) A fast, affordable, and semi-automatic design and fabrication method for directly encoding tunable, nonlinear stiffness into laminate robot legs; (2) An approach for modeling nonlinear stiffness at the spring level and understanding leg behavior at the system level; (3) A demonstration of how stiffness and nonlinearity play a role in jumping dynamics, verified through both component-level characterization and system-level jumping experiments.

In this paper, Sec. 2 presents the approach for designing, modeling, and optimizing the stiffness and dynamic motion of a jumping laminate robot leg. Section 3 develops a model that describes the vertical jumping of the leg actuated by a DC motor. Section 4 reports the design and prototype of a leg that can be tuned to one of six stiffness profiles. Section 5 provides details of the characterization and validation experiments performed on the leg. The experimental results are shown and discussed in Sec. 6. Lastly, Sec. 7 concludes the paper and points out future improvements.

## 2 Design Method

The design approach was structured so that legs resulting from the process exhibited basic locomotion capabilities and sufficient stiffness tunability while remaining as simple as possible. Thus, we chose legs that can extend and retract in the sagittal plane and exhibit series compliance, under the assumption that series compliance heavily influences the stability, efficiency, and performance of legged locomotion providing opportunities for further study. Rotational motors were selected to drive the leg because they are widely available in various dimensions, at different weights, and across a spectrum of performance. The leg is a five-layer laminate device with two outer, structural layers of the same material (sometimes at different thicknesses), two identical adhesive layers, and one flexible layer in the center.

**2.1 Stiffness.** As shown in Figs. 3(a) and 3(b), leg compliance principally originates in a triangle-shaped linkage, wherein one link is more flexible due to a section with thinner structural layers. When the three-link system is subjected to a torque, this section bends and the entire linkage behaves as a torsion spring.

The pseudo-rigid-body model (PRBM) for an end-loaded cantilever beam with end forces developed by Howell and Midha captures the stiffness and deformation of the flexible section, which is modeled as two rigid links of the same total length connected by a torsion spring [25]. The two subdivided links are then appended to stiffer extensions on each end. Thus, the entire spring may be modeled as a four-bar linkage with a torsion spring shown in Figs. 3(c) and 3(d). The spring constant is calculated by

$$k_s = \gamma K_\theta \frac{EI}{l_{A'C'}} \tag{1}$$

where  $K_{\theta}$  is the PRBM stiffness coefficient,  $\gamma$  is the proportion of the longer link of the two equivalent rigid links, E is the Young's modulus of the material,  $I = (wt^3)/12$  where w and t are the width and thickness of the flexible section respectively, and  $l_{A'C'}$  is the length of the flexible section. For common loading conditions,  $\gamma = 0.85$  and  $K_{\theta} = 2.65$  [26]. As a result, the lengths of the two rigid counterparts of AC are  $l_{AD} = l_{AA'} + (1 - \gamma)l_{A'C'}$  and  $l_{CD} = l_{CC'} + \gamma l_{A'C'}$ .

Since the potential nonlinear stiffness of the proposed spring cannot be described by Hooke's law, the force and deformation relationship is extended as

$$F = \operatorname{sign}(x)F_{\max} \left| \frac{kx}{F_{\max}} \right|^{a} \tag{2}$$

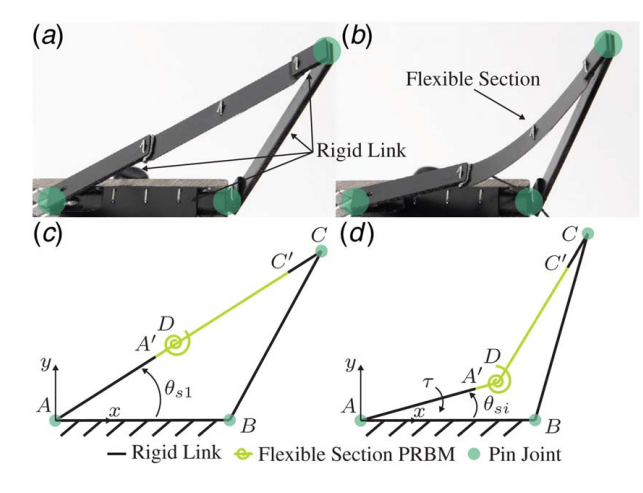


Fig. 3 (a) Photo of the laminate spring and (b) photo of the laminate spring under deformation. The string used to deform the spring is only for taking the photo and it is not present on the final device: (c) model of the laminate spring at rest and (d) model of the laminate spring under deformation.

where F and x represent either force and displacement or torque and rotation, k is the stiffness coefficient,  $F_{\rm max}$  is the maximum force output of the spring, and a is the term expressing the nonlinearity. We normalize nonlinearity against maximum force because the motor in our series of prototypes, which directly compresses the spring, is limited in the peak force it can deliver. In this way, the spring's maximum deformation range varies with the stiffness coefficient to  $F_{\rm max}/k$ . Increasing the nonlinearity term a from zero to one to infinity corresponds to changing the stiffness profile from initially hard to linear to initially soft, respectively, as shown in Fig. 1. This also implies that a must be increased by a larger amount when a > 1 to achieve the same curvedness compared to when a < 1.

To obtain the ideal spring geometry for a given stiffness profile, the stiffness error and spring mass was minimized according to the following cost function:

$$f_{s} = f_{s}(l_{AA'}, l_{AB}, l_{BC}, l_{A'C'}, w_{A'C'}, t_{A'C'}, d)$$

$$= \frac{1}{N_{s}} \sum_{i=1}^{N_{s}} |\tau_{i} - \tau'_{i}| + W_{s} m_{s}$$
(3)

where the link lengths l, flexible section width  $w_{A'C'}$ , thickness  $t_{A'C'}$ , and deformation direction d are the design variables.  $\tau_i$  represents the torque required to deform the spring from  $\theta_{s1}$  to  $\theta_{si}$ , as calculated by a static force analysis, and  $\tau_i'$  represents the torque calculated from a desired stiffness profile defined by Eq. (2).  $N_s$  is the number of discrete points compared when deforming the spring from  $\theta_{s1}$  to  $\theta_{s1} + \tau_{\text{max}}/k$ , and  $W_s$  is a weight constant that adjusts the relative importance of the spring mass  $m_s$  compared to stiffness error. The stiffness was only matched in compression because our spring design is intended to operate mostly in compression when integrated into the leg.

**2.2 Motion.** The other function of the leg is to convert the rotation of the motor into translation. A four-bar linkage was chosen because flexure joints in a laminate device most closely resemble pin joints in more traditional mechanisms and are simple to fabricate. It is also simple to connect its crank with the link *AB* of the spring to form the entire leg as shown in Fig. 1.

The laminate four-bar linkage was modeled as rigid links connected by pin joints as in Fig. 4. The linkage orientation  $\alpha$  is a dependent variable that can be determined by making sure the foot I is on the negative y-axis. The links FG and GI form a single link but are intentionally modeled as noncollinear to represent the joint offset caused by the connection between them and

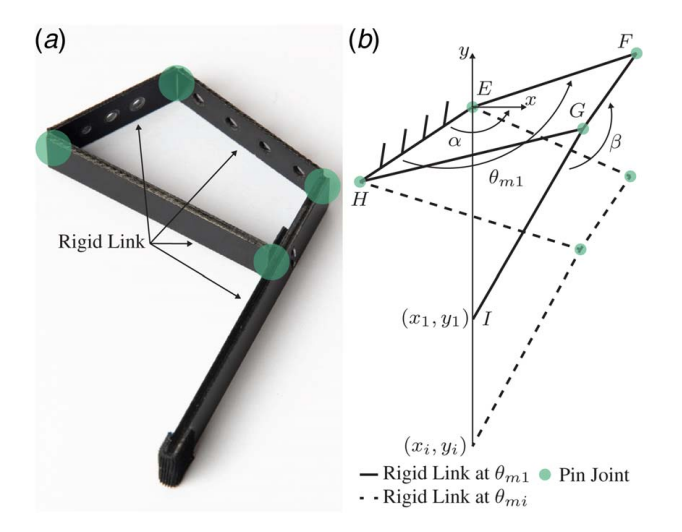


Fig. 4 (a) Photo of the four-bar linkage and (b) model of the four-bar linkage

the link GH on the real device. Their angle  $\beta$  depends on the device thickness and  $l_{GI}$ .

An optimization routine was used to find a design that keeps the foot trajectory as straight as possible when the crank is rotating; this is described by the cost function  $f_m$  and the desired foot trajectory  $y_i$ , with

$$f_m = f_m(\theta_{m1}, l_{EF}, l_{FD}, l_{GH}, l_{EH}, l_{GI}, c)$$

$$= \frac{1}{N_m} \sum_{i=1}^{N_m} |y_i - y_i'| + |x_i|$$
(4)

$$y_i' = r(\theta_{mi} - \theta_{m1}) + y_1$$
 (5)

where the design variables include initial crank angle,  $\theta_{m1}$ , link lengths l, and a variable c that indicates whether or not the linkage is in crossed form.  $x_i$  and  $y_i$  are calculated from the linkage kinematics,  $N_m$  represents the number of points compared along the trajectory from  $\theta_{m1}$  to  $\theta_{m1} + \Delta_{\theta_m}$ , and r is the virtual radius that maps the crank rotation into the foot displacement.

**2.3** Implementation. Several edge cases exist for motion and stiffness optimization. For example, it is possible that the combination of design variables does not form a valid four-bar linkage or triangle. Likewise, if  $\theta_{si}$  is too small, the links will hit each other. Furthermore, the spring can also be longer than the four-bar linkage and touches the ground during jumping. When these cases are encountered we return a large cost value. The four-bar linkage also needs to be designed before the spring so that the spring's size is properly constrained. In addition, for the discrete design variables including  $t_{A'C'}$ , d, and c, their continuous counterparts are converted by step functions. The values for all the design parameters are listed in Table 2. The entire process and calculation is coded in PYTHON. The differential evolution algorithm, available in the SciPy package is used to find the global minimum [27]. Once a spring and a four-bar linkage are determined, 3D models of the laminate devices are then created in their flattened state; these can be easily folded up for assembly with other components in CAD. A processing script, coded in PYTHON and based on Ref. [24], converts the design into cut files containing the cut patterns for each layer along with the cut geometry for releasing the laminate from its web.

## 3 Jumping Model

To verify that the nonlinear springs function as expected in dynamic scenarios, a model of the leg doing a vertical jump actuated by a DC motor was developed and compared against experimental data. We modeled only the stance phase of the jump, because all motion after the foot leaves the ground is ballistic, where leg design plays a significantly smaller role.

As shown in Fig. 5, the jumping leg consists of a body with a DC motor, a spring, a leg represented by a pinion and rack pair, and a foot. The motor spins the pinion through the torsion spring in series. The rack converts the rotation to translation and pushes against the ground. The foot is assumed to be always in contact with the ground, which was later confirmed from the slow-motion video of the actual jump. The equations of motion and the motor electrical system can be described as

$$I_m \ddot{\phi_m} = Ki - b_m \dot{\phi_m} - \tau_s - \tau_{mb} \tag{6}$$

$$\left(m_b + \frac{I_l}{r^2}\right)\ddot{y_b} = \frac{\tau_s}{r} - m_b g - F_{bb} \tag{7}$$

$$\phi_l = y_b/r \tag{8}$$

$$\phi_s = \phi_m - \phi_l \tag{9}$$

$$L\dot{i} = V - K\dot{\phi_m} - Ri \tag{10}$$

where  $m_b$  is the body mass,  $I_m$  is the motor inertia,  $I_l$  is the leg inertia, K, R, L, V, and  $b_m$  are the motor torque constant, resistance, inductance, voltage, and damping, r is the moment arm of the pinion,  $\phi_m$ ,  $\phi_l$ , and  $\phi_s$  are the motor angle, the pinion angle, and the spring deformation angle, and  $y_b$  is the body displacement. Additionally,  $\tau_s$  is the nonlinear spring torque similar to Eq. (2);  $\tau_{mb}$  represents the joint limit that prevents the motor from rotating past  $\Delta_{\theta_m}$ ;  $F_{bb}$  is caused by another joint limit that prevents the leg from retracting beyond defined starting length. They are formulated

$$\tau_s = \operatorname{sign}(\phi_s) \tau_{\max} \left| \frac{k\phi_s}{\tau_{\max}} \right|^a + b_s \dot{\phi}_s \tag{11}$$

$$\tau_{mb} = \begin{cases} k_{mb}(\phi_m - \Delta_{\theta_m}) + b_{mb}\dot{\phi_m}, & \phi_m > \Delta_{\theta_m} \\ 0, & \text{otherwise} \end{cases}$$
(12)

$$F_{bb} = \begin{cases} k_{bb} y_b, & y_b < 0\\ 0, & \text{otherwise} \end{cases}$$
 (13)

where  $b_s$  is the damping of the spring,  $k_{mb}$  and  $b_{mb}$  simulate the spring and damping coefficient of the motor joint limit, and  $k_{bb}$  is for the leg joint limit. All initial states are set to zero except  $y_b =$  $-m_b g/k_{bb}$ . The leg leaves the ground when the normal force experienced by the foot,  $N = \tau_s/r - \ddot{y_b}I_l/r^2 + m_f g - F_{bb}$ , reaches zero.

## 4 Prototypes

Fiberglass sheets<sup>2</sup> have been selected as structural layers of the laminate because they have a high yield strength and are flexible, easy to cut, affordable, and come in a variety of thicknesses. Sheets at 0.27 mm and 0.45 mm are used for the spring's structural layer with the flexible section. The 0.83 mm fiberglass is used for the other structural layer without the flexible section, providing enough rigidity without adding too much weight. The four-bar linkage uses 0.45 mm and 0.83 mm fiberglass. The Young's modulus E of all fiberglass sheets was measured at around 10.3 GPa based on preliminary testing. The 0.05 mm polyester sheet<sup>3</sup> is selected for the middle flexure layer, while the 0.015 mm heat-activated adhesive is used as the adhesive layer.

Six different spring prototypes and one four-bar linkage were designed and fabricated to form six leg variants with different stiffness profiles. To be noted, our proposed method mainly follows the third approach of tuning and integrating leg stiffness discussed in Sec. 1. The spring in the leg design is not discrete because it is made of the same materials of the four-bar linkage and can be easily combined into a monolithic mechanism. For the purpose of this study, we kept the parts modular to reduce the amount of fabrication required and to maintain consistency within the four-bar linkage. In the future when developing an entire multi-legged robot, the spring will be embedded into the leg to avoid the extra mass and complexity of keeping all parts modular. The springs were divided into two groups of stiffness coefficients at  $k = \{0.1,$ 0.2 Nm/rad and three nonlinearity factors at  $a = \{0.5, 1.0, 2.0\}$ . The maximum torque was set to  $\tau_{\text{max}} = 0.06 \,\text{Nm}$ , resulting in 0.3 or 0.6 rad spring travel range. These values represent roughly the boundary of the feasible stiffness design space for the proposed method, geometry, and material selection. The length of the flexible section was limited to a small range to keep all springs similar in

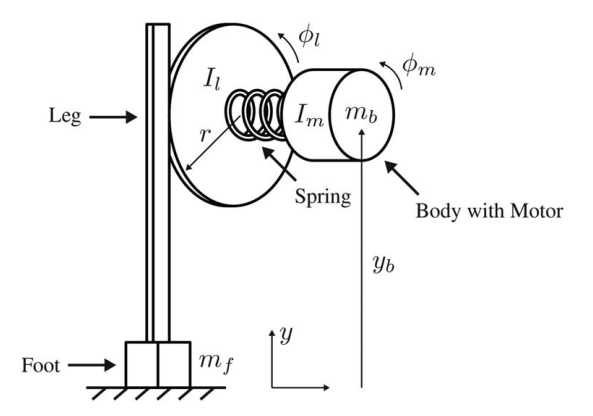


Fig. 5 The jumping leg model consists of a body with a DC motor, a spring, a leg represented by a pinion and rack pair, and a foot

size and mass. The resulting spring designs are shown in Table 1; the stiffness profiles predicted by the design model are plotted in Fig. 8. The design parameters for the four-bar linkage were determined by balancing the needs of a straight foot trajectory, a low mass linkage, and a large crank rotation range. The final design has a crank rotation range of  $\Delta_{\theta_m} = 1.5 \,\text{rad}$  and a virtual radius of  $r = 40 \,\mathrm{mm}$ , as shown in Fig. 6.

A close-up photo of the fully assembled device is shown in Fig. 1(a). To reduce the footprint of the spring, the flexible section is divided in pieces and stacked in the direction of layer thickness. An additional layer of 0.83 mm fiberglass sheet is added to the link FG and GI of the four-bar linkage to further increase the rigidity. To form a leg, the spring and linkage are then connected together with fiberglass sheets, plastic rivets,<sup>5</sup> and staples. This allows us to quickly swap springs and test the leg at different stiffness profiles. A small strip of friction tape<sup>6</sup> is applied to the foot. 3D printed parts and screws are used to attach a micro-metal gear motor with 75:1 ratio. The 3D printed parts also have joint limits to constrain leg travel and the range of allowable motor rotation. The entire leg system weighs ~28 g, consisting of the motor at  $10 \, \text{g}$  and the laminate mechanism at  $\sim 15 \, \text{g}$ .

#### 5 Experiments

Multiple experiments were carried out to fully evaluate the prototypes. The stiffness profiles of all six springs were measured under static loading conditions. In this experiment as shown in Fig. 7(a), the link AB of the spring is fixed onto a force sensor<sup>8</sup> while a robot arm<sup>9</sup> pushes the link AA' around an axis that is perpendicular to the ground and goes through the spring origin. The robot is commanded to rotate 0.01 rad and wait 1 s at each step until the spring's maximum deformation is reached. The torque exerted on the sensor and the robot's rotation around the axis are then recorded at  $\sim 1000$  Hz. Each experiment is then repeated three times. In postprocessing, only the settled part of the rotation and torque data for each step is averaged and used. The rotation data are also offset by the angle where the robot begins to deform the spring, which is determined by obtaining the angle where the torque first exceeds 0.001 Nm. Three trials for each spring are then interpolated and averaged to form a single stiffness curve. Plots of all the curves can be seen in Fig. 8. The stiffness coefficient and nonlinearity of the actual devices are then found with curve fitting, which are plotted in Fig. 9.

<sup>&</sup>lt;sup>2</sup>ACP Composites G-10/FR4.

<sup>&</sup>lt;sup>2</sup>Grafix Clear Dura-Lar.

<sup>&</sup>lt;sup>4</sup>Drytac MHA.

<sup>&</sup>lt;sup>5</sup>Heyco Products HEYClip Snap Rivets 9030.

<sup>&</sup>lt;sup>6</sup>3M Gripping Material TB641.

<sup>&</sup>lt;sup>7</sup>Pololu 3064

ATI Industrial Automation Mini40 IP65/IP68.

<sup>&</sup>lt;sup>9</sup>Universal Robots UR5e.

Table 1 Spring designs and properties

Goal stiffness coefficient, Nm/rad	0.1			0.2		
Goal nonlinearity	0.5	1	2	0.5	1	2
Shape	- At Rest	Deformed to 7,	max/k — Input/O	Output Link — a =	$=0.5 \longrightarrow a = 1.0$	10mm - a = 2.0
Device photo	1			1		10mm
Flexible section width/thickness, mm Spring/Leg mass, g Damping coefficient, $1 \times 10^{-4}$ Nm/ (rad/s)	21.3/0.45 5.33/28.5 16.3	12.2/0.45 4.24/27.2 12.9	13.8/0.27 4.23/27.2 2.25	31.1/0.45 5.94/29.2 22.8	24.2/0.45 4.72/27.7 15.8	22.8/0.27 4.68/27.7 5.74

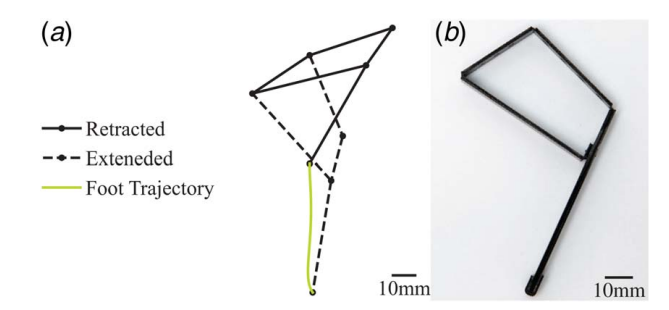


Fig. 6 (a) Shape of the four-bar linkage design and (b) photo of the four-bar linkage device

The stiffness profile of the full leg is often slightly different from just the triangular spring; another set of static stiffness experiments for all the leg variants was thus conducted. In these experiments as shown in Fig. 7(b), the link EH of the leg is fixed to the ground and the link EF is set but not fixed to the  $\theta_{m1}$  starting pose with the foot slightly touching the force sensor. The robot arm then pushes the link AA' in the same way as the previous tests so that the deformation of the spring causes a force to be applied to the sensor. The force and robot rotation are then recorded and processed in a similar fashion, except that an initial offset angle is selected at the point that the force first exceeds 0.05 N. To compare the spring and leg stiffness on the same plot (Fig. 8), an equivalent moment arm of 34 mm is used to compare force and torque; this value was selected because it minimizes the error between spring and leg stiffness.

Further experiments were performed to characterize the effective damping of the springs. In these experiments as shown in Fig. 7(c), the spring is fixed onto the ground with a  $10\,\mathrm{g}$  weight and a marker added to link AA'. The link is then deformed to its maximum angle and released manually. The oscillation of the weight is tracked and recorded by a motion capture system  $^{10}$  at  $360\,\mathrm{Hz}$ . Assuming the behavior is similar to a second-order linear spring, damper, and mass system, the damping coefficients were derived from the second peak to the end of the recorded oscillation to avoid disturbances due to initial release. The results are listed in Table 1.

Vertical jumping experiments were then performed across all leg variants. In these experiments as shown in Fig. 7(d), the leg starts

at its fully retracted pose; the DC motor is then activated at 9 V for 0.5 s, fully extending the leg. The jump is guided by a plastic tube which slides along a pre-tensioned string. Although the tolerance between the tube and string's diameter is rather large and vibrations in the string are present during the ballistic phase, the system is able to produce relatively smooth, low-friction motion before the leg left the ground as shown in the Supplemental Video. 11 The same force sensor and motion capture system are used to record the ground reaction forces (GRF) at 1000 Hz and the body position at 360 Hz. Five jumps are recorded across each design variant. The body speed is calculated from the position data. The starting time of the jump is when the voltage is applied and the lift-off time is when the measured GRF became zero. Both the speed and GRF are forward-backward filtered with a second-order 20 Hz low-pass Butterworth filter. The data of the five trials are then interpolated and averaged as shown in Fig. 10. A high-frame-rate camera<sup>12</sup> also records the entire jumping process at 1000 fps. Key frames of one of the jumps are shown in Fig. 11 and the Supplemental Video<sup>13</sup> includes a jumping clip for every leg variant.

The motion of each leg variant was also simulated using the model developed in Sec. 3. In each simulation, the body mass is set to  $m_b = 20\,\mathrm{g}$  and the foot mass is set to  $m_f = 8\,\mathrm{g}$ . The inertia of the pinion,  $I_b$ , which is related to the spring and part of the four-bar linkage, is ignored because it is small compared to the reflected inertia of the motor. The simulation also uses the stiffness coefficient and nonlinearity factor of the leg and damping coefficient of the spring measured previously. The DC motor parameters are obtained from an experimental characterization. The radius of the pinion is set to the same value as the virtual radius specified in the motion design. The values for all the model parameters are listed in Table 2. The equations were numerically solved using "RK45" [28], available in the SciPy package in PYTHON, at a maximum time-step of  $1 \times 10^{-4}$  s.

## 6 Results and Discussion

The stiffness profiles of the design goal, the model prediction, the spring, and the entire leg are plotted in Fig. 8. It is clear that the geometry of the proposed spring affects both of its stiffness coefficient and nonlinearity factor. Our proposed model captures

<sup>&</sup>lt;sup>10</sup>NaturalPoint OptiTrack Prime 17W.

<sup>11</sup>https://youtu.be/RLCke-TzDjA

<sup>&</sup>lt;sup>12</sup>Sanstreak Corp Edgertronic SC1.

<sup>&</sup>lt;sup>13</sup>See Note 11.

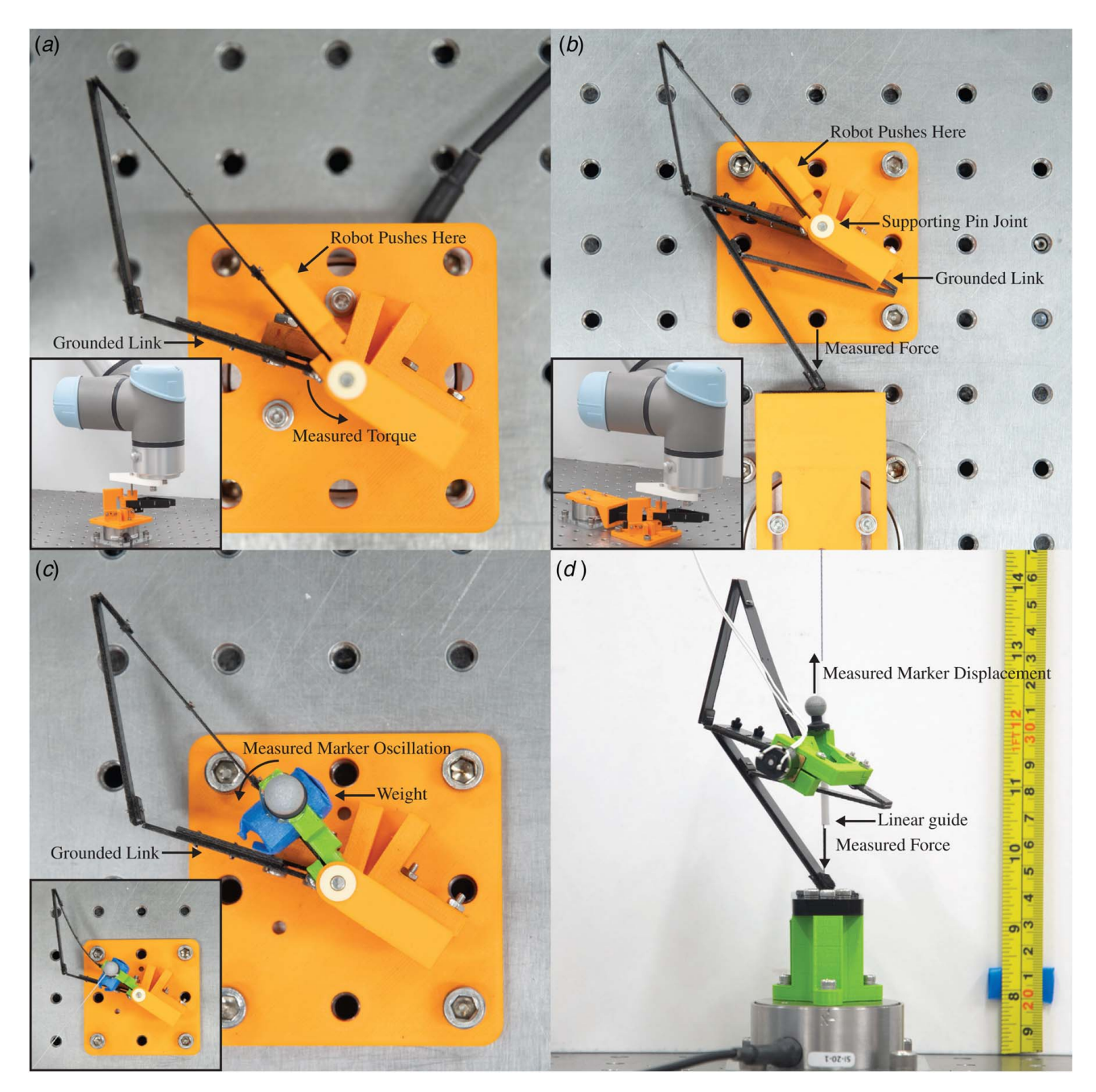


Fig. 7 Experimental setups for (a) the spring static stiffness, (b) the leg static stiffness, (c) the spring damping coefficient, and (d) the leg jumping test

this relationship well, and the design method is capable of tuning the stiffness profile on demand. Table 1 further shows that springs with the same nonlinearity factor have very similar geometric shapes. For linear stiffness, the spring is similar to a slim isosceles triangle. As the stiffness becomes nonlinear, the shape turns into an obtuse triangle. Depending on whether the spring is deformed toward or away from the grounded link, the initially soft or initially hard stiffness curves can be achieved. Conceptually, given a torque applied to the input link, the difference in shape alters the ratio between the tangential and normal force applied to the output link. As the spring is deformed, the ratio also continues to change and results in the nonlinear stiffness curve. The stiffness coefficient is driven primarily by the width of the flexible section, while the thickness of the flexible section determines the maximum or minimum "local" stiffness one spring can achieve. For example, since an initially soft spring has a very

small slope when slightly deformed, a thinner fiberglass sheet has to be used.

As illustrated in Fig. 9, the achieved range of stiffness profiles for actual springs and legs is smaller, even though the model predicts relatively large coverage across the goal design space. This is mainly because the remaining links in the system are not rigid enough and the flexure joints have additional, unintended compliance, unlike ideal pin joints. We confirmed this by comparing the stiffness profiles of four variants of the  $k\!=\!0.2$  and  $a\!=\!0.5$  spring design, among which three of them are laminates but with different width of the supposedly-rigid links and one is a closer-to-ideal 3D printed version with all joints supported by bearings and only the flexible section made from fiberglass. Details are omitted here to stay within the page limit and focus on the main topic. Material variation and fabrication inaccuracy also play a role in the deviation observed. The actual devices exhibit less nonlinearity than the

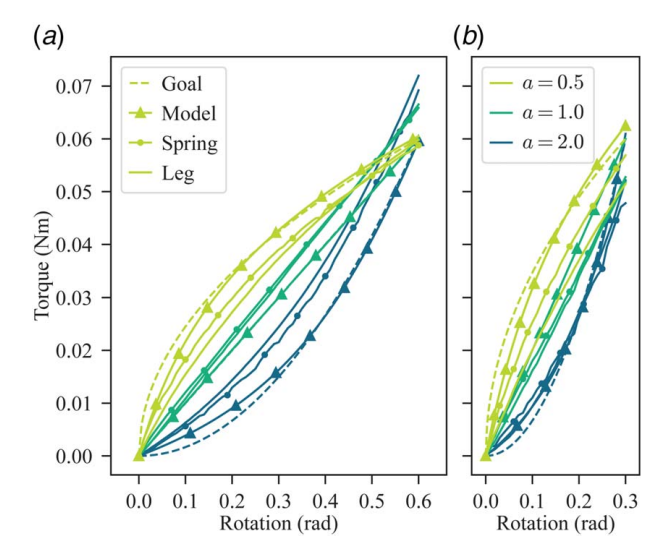


Fig. 8 Plots of tuned stiffness profiles of the robot leg, each with a comparison across the design goal, model prediction, individual spring, and entire leg. It demonstrates that both stiffness coefficient and nonlinearity are tunable for the proposed spring and leg design: (a) k=0.1 Nm/rad and (b) k=0.2 Nm/rad

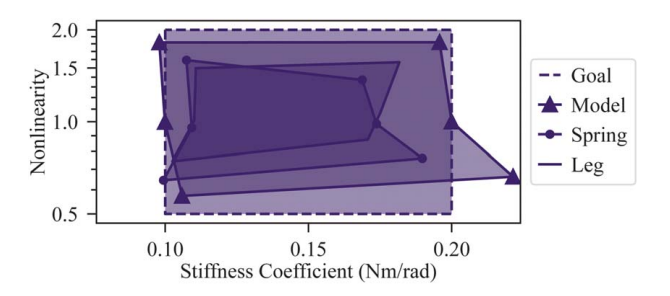


Fig. 9 Plot of the achievable design space of the robot leg. There is a trend of shrinkage from the design goal to model prediction to individual spring to entire leg.

model; this effect is worse for the entire leg than the spring. For both initially hard springs, the stiffness profiles of the entire legs are less nonlinear than their springs alone. The range of stiffness coefficients for real devices is also smaller, though it matches better than the nonlinearity factor. In the worst case, the lower bound is 11.0% higher for an initially soft spring and the upper bound is 14.5% smaller for an initially hard spring.

The differences between springs' damping coefficients can be quite significant, as shown in Table 1; they are clearly related to differences in geometry. The springs with thinner flexible sections have smaller damping coefficients; for springs of the same thickness, the damping coefficient is proportional to the width of the flexible section.

For the vertical jumping simulation and experiment, the body speed, GRF, and the power output are displayed in Fig. 10. The "power output" represents the power received by the leg; it is approximated from the product of body speed and GRF. The reasonable agreement across the results shows that the characterization method of the springs is valid and that the jumping model captures the key behaviors. It also affirms our hypothesis that leg stiffness can be tuned to achieve different performances. In fact, the liftoff speed of a leg with stiffness k = 0.1 and nonlinearity of a = 2.0 is 17.7% larger than a leg with stiffness of k = 0.2 and nonlinearity of a = 0.5, considering a relatively small difference in mass. Peak power output can also differ as much as 19.4%. More interestingly, there is a nearly linear relationship between peak power output and nonlinearity in both simulation and experiment, as shown in Fig. 12.

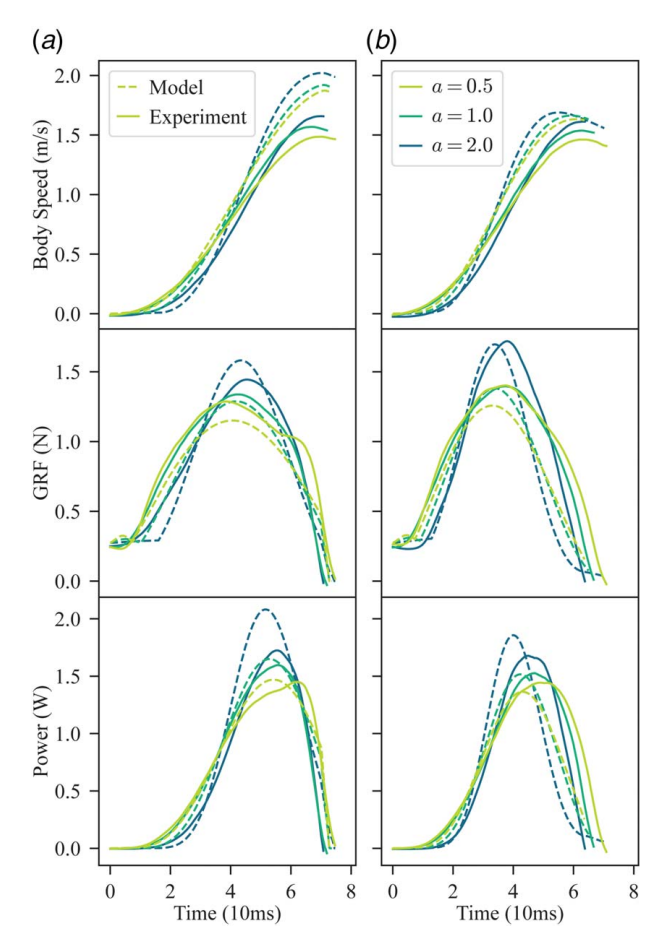


Fig. 10 Plots of body speed, GRF, and power of the robot leg jumping with different stiffness profiles. Both simulation of the model and experiment data are plotted. They are in close agreement especially on the correlation between nonlinearity and peak power output: (a) k = 0.1 Nm/rad and (b) k = 0.2 Nm/rad

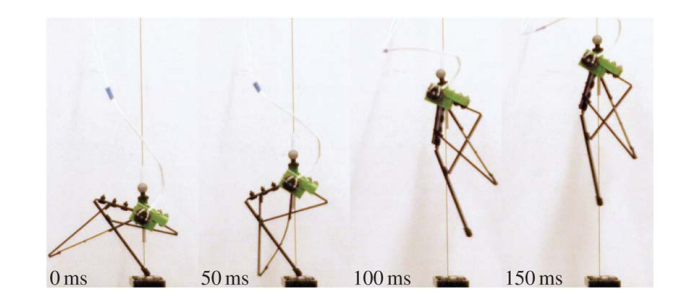


Fig. 11 Key frames of one of the jumping trials. The leg has a stiffness profile of k = 0.1 Nm/rad and a = 0.5.

Such relationships are not caused by the damping of the springs, since the simulation without damping produces similar results. Although a larger stiffness coefficient and nonlinearity search space might lead to further improvement in jumping performance theoretically, it is difficult to achieve in practice because the goal design space for this study is already out of reach for the selected design, geometry, and material as previously mentioned in Fig. 9. Additionally, some parameters that could significantly impact the performance such as the mass and damping are dependent and not individually tunable hinted by Table 1. Nevertheless, we do intend to explore techniques that could widen the achievable design space in the future.

Table 2 List of parameters and their values

Parameter	Value	Unit	
	Stiffness design		
$l_{AA'}$	[10, 30]	mm	
$l_{AB}, l_{BC}$	[20, 80]	mm	
$l_{A'C'}$	[40, 50]	mm	
$W_{A'C'}$	[10, 40]	mm	
$l_{C'C}$	10	mm	
$t_{A'C'}$	{0.27, 0.45}	mm	
$t_{AA'}$ , $t_{AB}$ , $t_{BC}$ , $t_{CC'}$	$0.91 + t_{A'C'}$	mm	
d	$\{-1, 1\}$		
$N_s$	50		
$W_s$	1	Nm/kg	
E	10.3	GPa	
$\rho$	1820	kg/m <sup>3</sup>	
γ	0.85		
$K_{\theta}$	2.65		
$ au_{ m max}$	0.06	Nm	
k	{0.1, 0.2}	Nm/rad	
a	{0.5, 1,2}	Motion design	
	Motion design		
$\theta_{m1}$	$[-\pi, \pi]$	rad	
$l_{EF}, l_{FG}, l_{GH}, l_{EH}, l_{GI}$	[10, 70]	mm	
$t_{EF}$ , $t_{FG}$ , $t_{GH}$ , $t_{EH}$ , $t_{GI}$	1.36	mm	
C	$\{-1, 1\}$		
r	40	mm	
$\Delta_{ heta_m}$	1.5	rad	
$N_m$	50		
	Jumping model		
K	0.122	Nm/A	
L	$580 \times 10^{-6}$	Н	
R	10.9	Ohm	
V	9	V	
$b_m$	$2.48 \times 10^{-4}$	Nm/(rad/s)	
$m_h$	0.02	kg	
$m_f$	0.008	kg	
$I_m$	$8.02 \times 10^{-5}$	kgm <sup>2</sup>	
$I_l$	0	kgm <sup>2</sup>	
$\vec{k}_{mb}$	10	Nm/rad	
$b_{mb}$	0.1	Nm/(rad/s)	
$k_{bb}$	5000	N/m	
g	9.81	$m/s^2$	

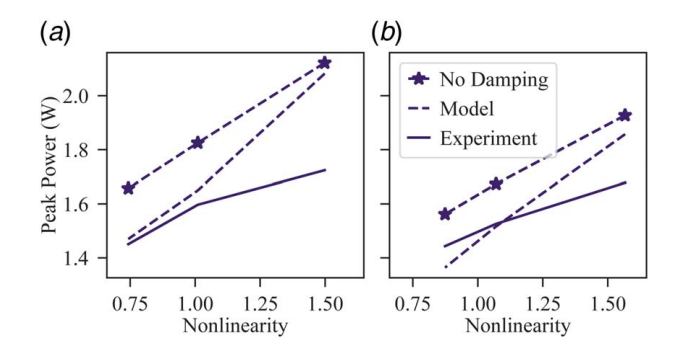


Fig. 12 Plots of the relationship between the peak power of the vertical jump and the leg stiffness profile. For both stiffness coefficients, the peak power is linearly proportional to the nonlinearity: (a)  $k=0.1\ \mbox{Nm/rad}$  and (b)  $k=0.2\ \mbox{Nm/rad}$ 

## 7 Conclusions

The origami-inspired laminate design and fabrication method is a powerful tool for quickly producing low-cost and diverse compliant robot legs. The proposed design, modeling, and optimization approach enables one to tune both the stiffness and nonlinearity of a robot leg from only a few design parameters, without any additional manual design steps. Once the design scripts were written and CAD models parameterized, it took only  $\sim$ 2 h to generate and fabricate all laminate components for all six variants. Our results also

demonstrate significant performance improvements through tuning these parameters via a series of vertical jumping experiments.

Several shortcomings will be addressed in future work. First, the achievable design space is rather small compared to the predicted space. The simplest solution is to utilize more complex crosssectional profiles to stiffen links, via folding or other means. Another option is to explore a wider range of materials to expand our range of available stiffnesses. On the other hand, instead of increasing complexity by stiffening inherently soft systems, we should also consider the advantages of keeping the leg design as simple as possible and optimizing our design to account for the parasitic compliance found in our current materials. Since our robots can be built quickly and affordably, this enables us to collect more data using real devices. Future work will explore machine learning techniques that can bridge the sim-to-real gap using experimental data, potentially avoiding the "arms-race" of making stiffer, larger, and thus more massive devices. Other differences between simulation and reality can be attributed to the relatively high inertia of the leg, and interference from the linear guide. This issue can be mitigated by carefully balancing the mass distribution of the entire robot system or scaling the system up.

This paper serves as a starting point of encoding tunable stiffness directly into laminate robot legs. This method lowers the barrier associated with studying the role of stiffness and nonlinearity in legged locomotion. It is our aim that this approach leads to more affordable, legged robot designs that can be easily tuned for novel applications and scenarios.

#### Acknowledgment

The authors would like to thank Yuhao Jiang for his assistance in photographing the devices and experiment setups. The authors would also like to thank the Robotics and Intelligent Systems Laboratory at Arizona State University for providing the high-frame-rate camera.

This material is based upon work supported by the National Science Foundation under Grant No. 1944789.

## **Conflict of Interest**

There are no conflicts of interest.

#### **Data Availability Statement**

The datasets generated and supporting the findings of this article are obtainable from the corresponding author upon reasonable request.

## References

- Blickhan, R., and Full, R., 1993, "Similarity in Multilegged Locomotion: Bouncing Like a Monopode," J. Compar. Physiol. A, 173(5), pp. 509-517.
- [2] Full, R., and Koditschek, D., 1999, "Templates and Anchors: Neuromechanical Hypotheses of Legged Locomotion on Land," J. Exp. Biol., 202(23), pp. 3325–3332.
- [3] Roberts, T. J., and Azizi, E., 2011, "Flexible Mechanisms: The Diverse Roles of Biological Springs in Vertebrate Movement," J. Exp. Biol., 214(3), pp. 353–361.
- [4] Saranli, U., Buehler, M., and Koditschek, D. E., 2001, "RHex: A Simple and Highly Mobile Hexapod Robot," Int. J. Robot. Res., 20(7), pp. 616–631.
- [5] Kim, S., Clark, J. E., and Cutkosky, M. R., 2006, "iSprawl: Design and Tuning for High-Speed Autonomous Open-Loop Running," Int. J. Robot. Res., 25(9), pp. 903–912.
- [6] Birkmeyer, P., Peterson, K., and Fearing, R. S., 2009, "DASH: A Dynamic 16g Hexapedal Robot," 2009 IEEE/RSJ International Conference on Intelligent Robots and Systems, St. Louis, MO, Oct. 10–15, IEEE, pp. 2683–2689.
- [7] Spröwitz, A., Tuleu, A., Vespignani, M., Ajallooeian, M., Badri, E., and Ijspeert, A. J., 2013, "Towards Dynamic Trot Gait Locomotion: Design, Control, and Experiments With Cheetah-Cub, A Compliant Quadruped Robot," Int. J. Robot. Res., 32(8), pp. 932–950.
- [8] Haldane, D. W., Plecnik, M. M., Yim, J. K., and Fearing, R. S., 2016, "Robotic Vertical Jumping Agility Via Series-Elastic Power Modulation," Sci. Robot., 1(1), p. eaag2048.

- [9] Hubicki, C., Grimes, J., Jones, M., Renjewski, D., Spröwitz, A., Abate, A., and Hurst, J., 2016, "ATRIAS: Design and Validation of a Tether-Free 3D-Capable Spring-Mass Bipedal Robot," Int. J. Robot. Res., 35(12), pp. 1497–1521.
- [10] Badri-Spröwitz, A., Aghamaleki Sarvestani, A., Sitti, M., and Daley, M. A., 2022, "BirdBot Achieves Energy-Efficient Gait With Minimal Control Using Avian-Inspired Leg Clutching," Sci. Robot., 7(64), p. eabg4055.
- [11] Galloway, K. C., Clark, J. E., Yim, M., and Koditschek, D. E., 2011, "Experimental Investigations Into the Role of Passive Variable Compliant Legs for Dynamic Robotic Locomotion," 2011 IEEE International Conference on Robotics and Automation, Shanghai, China, May 9–13, IEEE, pp. 1243–1249.
- [12] Sadeghi, S., Allison, S. R., Bestill, B., and Li, S., 2021, "TMP Origami Jumping Mechanism With Nonlinear Stiffness," Smart Mater. Struct., 30(6), p. 065002.
- [13] Hawkes, E. W., Xiao, C., Peloquin, R. -A., Keeley, C., Begley, M. R., Pope, M. T., and Niemeyer, G., 2022, "Engineered Jumpers Overcome Biological Limits Via Work Multiplication," Nature, 604(7907), pp. 657–661.
- [14] Owaki, D., and Ishiguro, A., 2006, "Enhancing Stability of a Passive Dynamic Running Biped by Exploiting a Nonlinear Spring," 2006 IEEE/RSJ International Conference on Intelligent Robots and Systems, Beijing, China, Oct. 9–15, IEEE, pp. 4923–4928.
- [15] Yu, H., Li, M., and Cai, H., 2013, "Analysis on the Performance of the SLIP Runner With Nonlinear Spring Leg," Chin. J. Mech. Eng., 26(5), pp. 892–899.
- [16] Plecnik, M. M., Haldane, D. W., Yim, J. K., and Fearing, R. S., 2017, "Design Exploration and Kinematic Tuning of a Power Modulating Jumping Monopod," ASME J. Mech. Rob., 9(1), p. 011009.
- [17] Galloway, K. C., Clark, J. E., and Koditschek, D. E., 2013, "Variable Stiffness Legs for Robust, Efficient, and Stable Dynamic Running," ASME J. Mech. Rob., 5(1), p. 011009.
- [18] Kalouche, S., 2017, "GOAT: A Legged Robot With 3D Agility and Virtual Compliance," 2017 IEEE/RSJ International Conference on Intelligent Robots and Systems (IROS), Vancouver, BC, Canada, Sept. 24–28, IEEE, pp. 4110– 4117.

- [19] Grimminger, F., Meduri, A., Khadiv, M., Viereck, J., Wuthrich, M., Naveau, M., Berenz, V., et al. 2020, "An Open Torque-Controlled Modular Robot Architecture for Legged Locomotion Research," IEEE Robot. Autom. Lett., 5(2), pp. 3650–3657.
- [20] Zhang, M., Fang, L., Sun, F., and Oka, K., 2019, "A Novel Wire-Driven Variable-Stiffness Joint Based on a Permanent Magnetic Mechanism," ASME J. Mech. Rob., 11(5), p. 051001.
- [21] Yu, J., Zhao, Y., Chen, G., Gu, Y., Wang, C., and Huang, S., 2019, "Realizing Controllable Physical Interaction Based on an Electromagnetic Variable Stiffness Joint," ASME J. Mech. Rob., 11(5), p. 054501.
- [22] Basu, A., Jujjavarapu, S. S., and Esfahani, E. T., 2020, "Design of a Novel Variable Stiffness Active Ankle Foot Orthosis Using Permanent Magnets for Drop Foot Assistance," Volume 10: 44th Mechanisms and Robotics Conference (MR), Virtual, Online, Aug. 17–19, American Society of Mechanical Engineers.
- [23] Faal, S. G., Chen, F., Tao, W., Agheli, M., Tasdighikalat, S., and Onal, C. D., 2016, "Hierarchical Kinematic Design of Foldable Hexapedal Locomotion Platforms," ASME J. Mech. Rob., 8(1), p. 011005.
- [24] Aukes, D. M., Goldberg, B., Cutkosky, M. R., and Wood, R. J., 2014, "An Analytic Framework for Developing Inherently-Manufacturable Pop-Up Laminate Devices," Smart Mater. Struct., 23(9), p. 094013.
- [25] Howell, L. L., and Midha, A., 1995, "Parametric Deflection Approximations for End-Loaded, Large-Deflection Beams in Compliant Mechanisms," ASME J. Mech. Des., 117(1), pp. 156–165.
- [26] Howell, L. L., Midha, A., and Norton, T. W., 1996, "Evaluation of Equivalent Spring Stiffness for Use in a Pseudo-Rigid-Body Model of Large-Deflection Compliant Mechanisms," ASME J. Mech. Des., 118(1), pp. 126–131.
- [27] Storn, R., and Price, K., 1997, "Differential Evolution—A Simple and Efficient Heuristic for Global Optimization Over Continuous Spaces," J. Global Optim., 11(4), pp. 341–359.
- [28] Dormand, J., and Prince, P., 1980, "A Family of Embedded Runge-Kutta Formulae," J. Comput. Appl. Math., 6(1), pp. 19–26.